



<http://www.diva-portal.org>

Postprint

This is the accepted version of a paper published in *Powder Technology*. This paper has been peer-reviewed but does not include the final publisher proof-corrections or journal pagination.

Citation for the original published paper (version of record):

Persson, A-S., Frenning, G. (2015)

An experimental evaluation of discrete element simulations of confined powder compression using an extended truncated-sphere model

*Powder Technology*, 284: 257-264

<https://doi.org/10.1016/j.powtec.2015.06.053>

Access to the published version may require subscription.

N.B. When citing this work, cite the original published paper.

Permanent link to this version:

<http://urn.kb.se/resolve?urn=urn:nbn:se:uu:diva-264807>

**An experimental evaluation of discrete element simulations of confined powder compression using an extended truncated-sphere model**

Ann-Sofie Persson\* and Göran Frenning

Uppsala University, Department of Pharmacy, Uppsala Biomedical Centre, P.O. Box 580, SE-751 23 Uppsala, Sweden.

\*Corresponding author:

E-mail: [ann-sofie.persson@farmaci.uu.se](mailto:ann-sofie.persson@farmaci.uu.se), Fax: +46 471 42 23, Phone: +46 18 471 49 78

## 1. Introduction

A considerable amount of research done in the pharmaceutical area has during many years focused on reducing the variability of products such as tablets manufactured by confined compression. It is therefore of utmost importance to gain an understanding of the underlying causes for the variation. Significant progress has been made by numerical methods but an improved understanding of the compression process including essential parameters for accurate descriptions of the various stages during compression is still needed. A promising and important tool often used for simulations in the pharmaceutical sciences is the discrete element method (DEM) [1]. The DEM enables simulations at the particulate level and uses a soft-particle approach where the contacts are modelled by a particle overlap.

The most commonly used contact models in DEM simulations of confined compression of granular materials are of an elastoplastic or a purely plastic type. Well-known examples include the model proposed by Storåkers et al. [2] that emanates from a similarity analysis of inelastic contacts, the model put forward by Thornton and Ning [3] that is based on a truncation of the Hertzian pressure distribution at a certain yield pressure, and the model of Vu-Quoc and Zhang [4] that utilises an additive decomposition of the contact radius into elastic and plastic parts. A more recent example is the model developed by Brake [5]. These models generally predict a largely linear increase in the contact force with increasing strain, except at very small strains, where the elastic Hertzian response makes the force–displacement relation nonlinear. In addition, simplified hysteretic spring models are sometimes also used, as originally proposed by Walton and Braun [6] and elaborated upon by Luding et al. [7]. Such models also predict a linear increase in force during loading.

However, the inherent assumption of contact independence made in the DEM and the aforementioned contact models is not justified at the large strains occurring during the late stage of compression (exceeding relative densities of about 0.8) [8, 9], rendering simulations of the elastic compact deformation problematic. This issue has been addressed in several ways. The analytical model presented by Harthong et al., based on curve-fitting to a meshed discrete element (MDEM) compression simulation, satisfactorily described the large strain incompressibility in DEM simulations [10]. In the model, the change in local relative density during compression was calculated from the corresponding volume change of Voronoi cells. This model has further been elaborated upon by Jerier et al. [11] and Harthong et al. [12]. A related, nonlocal contact model was developed by Gonzalez and Cuitino [13] who utilised the superposition principle to infer contact interactions for purely elastic particles. To model the large strain incompressibility in an average sense, keeping the notion of independent contacts, a maximal plastic overlap was introduced in the truncated Hertzian contact model [3, 14]. The maximal plastic overlap defines the particle overlap at which elastic deformation is initiated [14]. A similar force–displacement relation was used by Olsson and Larsson [15] (cf. their Fig 9b) who interpreted the increased stiffness as resulting from hardening occurring at a certain magnitude of the plastic strain. An analytical model proposed by Frenning [16] accounts for contact dependence and highlights the bulk modulus and the particle hardness as important parameters for describing the contact pressure evolution at low and intermediate strains. As originally suggested by Arzt [17], the deformed particle shape was described as a truncated sphere. The potential of this truncated-sphere contact model was established by an adequate correspondence to finite element simulations. The bulk modulus is preferable over the Young’s modulus for defining the particle volume changes as the bulk modulus provides a measure of the resistance to hydrostatic particle compression. The plastic hardness is suitable for describing the local plastic deformation at particle contact. However, the truncated-sphere

model accounts only for the initial particle compression, i.e. before contact impingement occurs; thus limiting the plastic deformation propensity. To account for the plastic incompressibility evident at large strains an extension of the model with Voronoi cells is appropriate.

The aim of this work was to extend the truncated-sphere model [16] so that it can be used in DEM simulations of confined compression and to compare its predictions of bulk compression to experiments. Granulated powders comprising millimetre-sized granules of a ductile (formed from microcrystalline cellulose) or a ductile-brittle (formed from a mixture of microcrystalline cellulose and lactose) character were used as model systems.

## **2. Theory**

In our previous work [16], a simplified model of the response of elastoplastic particles subjected to multiple simultaneous contacts was proposed. The model rested on two key assumptions, namely that the deformed particle shape could be approximated as a truncated sphere and that the contact areas could be translated to contact forces via an effective hardness  $\bar{H}$ . Although these assumptions resulted in a model that adequately captured numerical data for small to moderate (volumetric) strains, extensions are needed for large strains for two primary reasons. Firstly, the contact areas cease to be circular because of contact impingement and, secondly, the average contact pressure will increase beyond the hardness as a result of particle confinement. Here, such an extension is presented that utilises Voronoi polyhedra to estimate the particle volume and contact areas at large strains. In addition, a modification of the model that allows for plastic volume reduction of porous particles is proposed. For

simplicity, we will assume that a mean contact pressure  $\bar{P}$  can be used to relate the contact area to the normal force throughout the deformation, and hence write

$$F_i = \bar{P}S_i, \quad (1)$$

where  $F_i$  and  $S_i$  are the normal force on and surface area of contact  $i$ , respectively.

Equation (1) represents an effective description that remains valid even though the contact pressure need not be uniform throughout the deformation.

*Contact pressure:* As illustrated in Fig. 1a, we consider the average contact pressure  $\bar{P}$  to be a function of the volume  $V$  of the Voronoi polyhedron and identify three regions separated by two limiting volumes  $V_1$  and  $V_2$ . For small volumetric strains, i.e., large values of  $(V > V_1)$ , the average contact pressure  $\bar{P}$  was put equal to  $\bar{H}$  as in the model in its original form. For large volumetric strains ( $V < V_2$ ), the determination of  $\bar{P}$  was based on the definition of the bulk modulus  $\kappa$  of the dense material constituting the granules, using the Voronoi volume  $V$  as an estimate of the current particle volume. An interpolation was used for intermediate volumetric strains ( $V_2 < V < V_1$ ). Specifically,  $\bar{P}$  was expressed as follows:

$$\bar{P} = \begin{cases} \bar{H} & \text{if } V > V_1 \\ \bar{H} + K(V_1 - V)^\alpha & \text{if } V_2 < V < V_1 \\ \kappa \left(1 - \frac{V}{V_s}\right) & \text{if } V < V_2 \end{cases}. \quad (2)$$

Here,  $K$  and  $\alpha$  are constants and  $V_s = (1 - \phi_0)V_{p0}$  is the volume of the solid material that constitute the particle ( $\phi_0$  and  $V_{p0}$  are the initial particle porosity and volume, respectively).

As already indicated,  $V_1$  and  $V_2$  denote the upper and lower limits of the region where the contact pressure is interpolated, respectively.

Assuming that the interpolation ends at a pressure-to-hardness-ratio  $\beta$  (i.e.,  $\bar{P}/\bar{H} = \beta$  at  $V = V_2$ ; see Fig. 1a), the limiting volume  $V_2$  can be expressed as

$$V_2 = \left(1 - \frac{\beta \bar{H}}{\kappa}\right) V_s \quad (3)$$

If one considers the exponent  $\alpha$  as a known parameter, the limiting volume  $V_1$  and the constant  $K$  can be determined from the condition that  $P$  and the derivative  $dP/dV$  both be continuous at  $V_2$ , implying that

$$V_1 = \left(1 - \frac{\bar{H}}{\kappa}\right) \alpha V_s - (\alpha - 1)V_2 \quad (4)$$

and

$$K = \frac{\kappa}{\alpha V_s (V_1 - V_2)^{\alpha-1}} \quad (5)$$

As shown in Fig. 1b, the numerical values  $\alpha = 5$  and  $\beta = 3$  were found to reproduce the numerical data presented in our previous work [16] and these values were therefore used throughout the simulations discussed below. The exponent  $\alpha$  can be considered as a shape parameter for the interpolation of the contact pressure between the plastic and elastic responses. Similarly, the parameter  $\beta$  describes the location of the interpolation.

*Contact areas:* As illustrated in Fig. 2 for the special case of hydrostatic triaxial loading, each contact was assumed to have a circular shape as long as the assumptions underlying the truncated-sphere model remain valid. Each contact area could hence be expressed as

$$S_i = \pi(R^2 - r_i^2) \quad (6)$$

where  $R$  is the radius of the truncated sphere and  $r_i$  is the distance from the particle centre to contact point  $i$ . The radius  $R$  was (for coordination numbers  $n_c \geq 2$ ; the initial particle radius  $R_{p0}$  was used for  $n_c = 1$ ) determined from an equation of the form [16]

$$2(n_c - 2)R^3 - A R^2 + B = 0 \quad (7)$$

where

$$A = (3 + \lambda) \sum_{i=1}^{n_c} r_i \quad (8)$$

and

$$B = 4R_{p0}^3 + (1 + \lambda) \sum_{i=1}^{n_c} r_i^3 \quad (9)$$

In the above expressions,  $\lambda$  is a parameter that accounts for the volume reduction of the particle. Volume reduction was assumed to be purely elastic in the original truncated-sphere model, in which  $\lambda = \bar{H}/\kappa$  [16]. As described below, a larger value of  $\lambda$  can be used for porous particles that may densify plastically.

When  $n_c = 2$ , Eq. (7) reduces to a quadratic equation with solution

$$R = \sqrt{B/A} \quad (10)$$

When  $n_c \geq 2$ , the solution of Eq. (7) can be expressed as [16]

$$R = Y \left\{ 2 \cos \left[ \frac{\arccos(X - 1) + \pi}{3} \right] + 1 \right\} \quad (11)$$

where  $X = 54(n_c - 2)^2 B/A^3$  and  $Y = A/[6(n_c - 2)]$ .

The assumptions underlying the truncated-sphere model are valid until the circular contact area touches the boundary of the corresponding face of the Voronoi polyhedron. For simplicity, the model was in this work assumed to be valid until a certain value of  $X$ , denoted by  $X_c$  and estimated from hydrostatic triaxial loading ( $n_c = 6$ ; see Fig. 2) as

$$X_c = \frac{16(9 - 4\sqrt{2} + 3\lambda)}{(3 + \lambda)^3} \quad (12)$$

The above estimate is most readily obtained by noting that Eq. (7) implies that  $X$  can be expressed as a function of  $R/A$ . For hydrostatic triaxial loading, Eq. (8) reduces to  $A = 6(3 + H/\kappa)r$ , where  $r$  denotes the common value of  $r_i$ . Since the the critical value of  $R$  in

this case is obtained when  $R = \sqrt{2}r$ , one finds that  $R/A = \sqrt{2}/[6(3 + \lambda)]$ , which produces Eq. (12).

The radius of the truncated sphere was linearly extrapolated beyond  $X_c$ , according to

$$R \approx R_c + \left(\frac{\partial R}{\partial A}\right)_c (A - A_c) + \left(\frac{\partial R}{\partial B}\right)_c (B - B_c), \quad (13)$$

where the subscript “c” indicates values at  $X_c$ . The extrapolation was in force until the contact area was as large as the area of the corresponding face of the Voronoi polyhedron, and after this junction, the face area was used instead (see Fig. 2). To obtain a continuous representation of the contact area, the extrapolated value of  $R$  was used in Eq. (6). Moreover, in order to avoid discontinuities resulting from changes in the coordination number, a record was kept of contacts that were established at  $X_c$ , and contributions from these contacts only were used to calculate  $A$  and  $B$  according to Eqs. (8) and (9).

As mentioned above, the original truncated-sphere model did account for elastic volume reduction, and the relative decrease in particle volume was shown to be proportional to  $\bar{H}/\kappa$  [16]. Hence, a value of  $\lambda > \bar{H}/\kappa$  would imply a volume reduction that exceeds the one resulting from purely elastic deformation. For this reason, a fairly straightforward generalisation to plastic volume reduction can be made, using a parameter  $\lambda$  rather than  $\bar{H}/\kappa$  in the equations that determine the radius of the truncated sphere, as done in this work. For porous particles,  $\lambda$  was determined from hydrostatic triaxial loading, assuming that a nonporous particle was obtained when the extrapolated contact area was as large as the area of each confining face. Thus, the extrapolation was in force for  $r_m < r < r_c$ , where  $r_c$  is the value of  $r$  at  $X_c$  and  $r_m$  can be determined as

$$r_m = \left(\frac{V_s}{8}\right)^{1/3} \quad (14)$$

As Eq. (12) shows, the value of  $\lambda$  affects  $X_c$  and hence also  $r_c$ . For a given initial porosity  $\phi_0$ , values of  $\lambda$  and  $r_c$  can be determined from the conditions that, firstly, the extrapolated area should equal  $4r_m^2$  when  $r = r_m$  and, secondly, that Eq. (7) should be fulfilled for  $r = r_c$ . It proves convenient to utilise the parameter  $\xi = (r_c - r_m)/R_{p0}$ , which generally is much smaller than unity (see below). After a rather lengthy calculation, one obtains the estimates

$$\lambda \approx \frac{1}{1 - \phi_0} - (3 - 2\sqrt{2}) - \frac{\pi}{6}(3 - \sqrt{2}) \quad (15)$$

and

$$\xi \approx \left(\frac{2}{3\lambda + 15 - 8\sqrt{2}}\right)^{1/3} - \left(\frac{\pi}{6}(1 - \phi_0)\right)^{1/3} \quad (16)$$

to the first order in  $\xi$ . As a consistency check, one may note that the value of  $\xi$  obtained from Eq. (16) is not larger than about 3%, irrespective of the initial porosity. The described procedure is sufficient for our purposes, but it can be noted that the analysis is not valid when the porosity is very small, since a negative value of  $\lambda$  would then be obtained ( $\lambda$  becomes negative when the porosity is smaller than about 0.2%). The reasons for this are twofold. First, the assumed kinematics with an extrapolation of  $R$  is only an approximation of the true kinematics. Second, only first order terms have been retained in the determination of  $\lambda$  according to Eq. (15). A pragmatic solution, utilised in this work, is to use the value obtained by Eq. (15) as long as this value exceeds  $\bar{H}/\kappa$  and to put  $\lambda$  equal to  $\bar{H}/\kappa$  otherwise.

### 3. Experimental

#### 3.1 Materials

Granules were prepared from microcrystalline cellulose powder (Avicel PH 101, FMC, Ireland) and lactose powder ( $\alpha$ -lactose monohydrate, Pharmatose 200 M, DMV, the Netherlands), hereafter referred to as MCC and LAC, respectively. The apparent density of the MCC and LAC powders were 1.58 and 1.54 g/cm<sup>3</sup>, respectively, as determined by Helium pycnometry (AccuPyc 1330, Micromeritics, USA;  $n = 2$  independent measurements with each measurement being an average of ten repeated cycles). The apparent density of binary powder mixtures ( $\rho_{\text{mix}}$ ) was calculated as described earlier [18]. Deionised water was used as granulation liquid. Potassium carbonate (Sigma-Aldrich, Germany) was used as a desiccant.

### **3.2 Granule preparation**

Granules based on MCC only and mixtures of MCC and LAC (in the proportions 1: 4 by weight) were prepared through granulation followed by extrusion-spheronisation according to Nordström et al. [19]. The powder was initially dry mixed for 3 min at 500 rpm in a high shear mixer (QMM-II, Donsmark Process Technology, Denmark). The granulation liquid was manually poured into the powder during continuous mixing at an approximate rate of 100 ml/min. Wet mixing was subsequently made for an additional 3 min at 500 rpm. The wet mass was directly extruded through holes 1.0 mm in diameter and 1.2 mm long (NICA System AB, model E140, Sweden) and spheronised for 3 min at approximately 850 rpm on a 32 cm diameter friction plate with a radially designed grid (NICA System AB, model S 320-450, Sweden). The granules were dried at room temperature for a minimum of three days. The size fraction 800-900  $\mu\text{m}$  was separated by dry sieving for 10 minutes with a relative agitation intensity of 50 (Retsch, Type RV, Germany) using sieves with square openings (Endecotts, United Kingdom). The separated size fraction was stored in a desiccator at room temperature

above a saturated solution of  $K_2CO_3$  (giving a relative humidity, RH, of ~40%) for at least 5 days prior to use.

### 3.3 Granule characterisation

*Size and shape analysis:* The median granule size ( $d_{50}$ ) was assessed by scanning separated granules ( $n > 1000$ ) using a flatbed scanner (Epson Perfection 1640SU Scanner, Seiko Epson Corp., Japan). Images of 1600 dpi resolution were captured and analysed with ImageJ [20]. The granule diameter was calculated from the projected circle area assuming spherical particles. Stereo microscopy images (Zeiss AxioCam ICc 5, Carl Zeiss AB, Sweden) were taken at 40 times magnification to enable visualisation of the granule shape.

*External surface area:* Steady-state permeametry was used to measure the granule volume-specific surface area ( $S_v$ ,  $n=3$ ). Granules (~9 g) were manually poured into a cylinder (diameter 11.42 mm and height 165 mm) and the height was recorded (Mitutoyo Digimatic, ID-C, Tokyo, Japan). Air flow of controlled rate (Brook flow meter, Brook Instruments B. V., the Netherlands) was allowed through the granule bed. The build-up pressure was measured from high to low flow rate using a manometer (P 200 S, Digitron Instrumentation Ltd, UK) and was used for calculation of the granule external surface area using the Kozeny-Carman equation and an aspect factor of 6, as described earlier [21].

*Effective granule density and granule porosity:* Low pressure mercury intrusion pycnometry (Autopore III 9420, Micromeritics, USA) was used to assess the effective granule density ( $\rho_{\text{eff}}$ ,  $n=3$ ) as previously described [22]. Prior to the measurements the granules were stored in a desiccator cabinet over  $P_2O_5$  (providing a RH of nearly 0%) at room temperature to

accelerate the degassing step. The intra-granular porosity was calculated as one minus the ratio between the effective and the apparent density.

*Bulk density:* The poured bulk density ( $\rho_{\text{bulk}}$ ,  $n=3$ ) was determined by pouring 50 mL granules through a funnel into a measuring cylinder (21.7 mm diameter) and weighing (Delta Range B3002, Mettler Toledo, Switzerland). The granule bed was subjected to 1250 taps (PharmaTest, PT-TD, Hainburg, Germany) in three steps (10, 500 and 1250 taps) to assess the tapped bulk density ( $\rho_{\text{tap}}$ ,  $n=3$ ) according to the European Pharmacopoeia [23]. Carr's compressibility index (CI) was calculated from the bulk and the tap densities in a standard manner [24].

*Unconfined single-granule compression:* Unconfined uniaxial compressions of single granules ( $n=50$ ) were performed using a Texture analyser (TA.HDi Texture Analyser, Stable Micro Systems, UK) with a 50 N (5 kg) load cell at a rate of 0.5 mm/s. The compressions were performed against a flat surface with a flat-faced movable upper probe (6 mm diameter). The compressions were allowed to proceed slightly beyond particle breakage i.e., forces exceeding the fracture force were applied. The particle hardness ( $H$ ) was estimated from the force vs. displacement curves in accordance with the Abbott–Firestone model [25, 26] as

$$H = \frac{k}{\pi R_{50}}, \quad (16)$$

where  $k$  is the slope of the plastic region of the force vs. displacement curve and  $R_{50}$  represents the median particle radius. As illustrated in Fig. 3, the slope was determined by linear regression in a displacement range between 15.8-35.4  $\mu\text{m}$  (3.4-7.5% strain;  $R^2 > 0.990$ ) for the MCC granules and 15.7-26.3  $\mu\text{m}$  (3-5% strain;  $R^2 > 0.982$ ) for the MCC/LAC granules. The obtained data was corrected for punch and machine deformation.

### **3.4 Confined granule bed compression**

Uniaxial compressions of 0.5 g granules were performed using a materials tester (Zwick Z100, Zwick/Roell GmbH & Co. KG, Ulm, Germany) equipped with a stationary lower and a movable upper punch (diameter 11.3 mm). The granule bed was subjected to a maximum load of 300 MPa with a compression rate of 25 mm/min. Prior to compression the particle-wall friction was reduced by lubrication of the punches and the matrix with 1% (w/w) magnesium stearate suspended in ethanol. The obtained data was corrected for punch and machine deformation [19].

## **4. Simulations**

Bulk compression simulations were performed for monodisperse spherical particles using a cylindrical geometry that matched the experiments with a mobile upper and a stationary lower boundary. The number of particles used in the simulations was 821 and 662 for the MCC and MCC/LAC granules, respectively, as calculated from the total granule mass, using the median diameter and effective density of the granules (Table 1). Initial packings were generated by letting particles with random initial velocities settle under the influence of gravity, until the kinetic energy was sufficiently dissipated. The initial extragranular porosity (i.e., voidage) of the thus formed packings was about 50%. In the bulk compression simulations, the normal forces were based on the extended truncated-sphere model described in Sec. 2. The model accounts for the expected response of elastoplastic particles subjected to multiple simultaneous contacts during loading but does, in its current form, not include any specific

unloading branch. However, this should be of little concern as long as monotonic loading is simulated.

As summarised in Table 1, simulations were performed both with and without an account of plastic volume reduction (in the latter case, the initial porosity of the granules was set to zero). As demonstrated in our previous work [16], the effective hardness  $\bar{H}$  represents an average value over a large deformation range that is lower than the actual hardness  $H$  (notice that  $\bar{H}/\sigma_y \approx 1.8$  in Fig. 1 rather than about 3). Hence,  $\bar{H}$  was in this work set to  $1.8/3 \times H = 0.6 \times H$ . For both pellet types, the bulk modulus was calculated from literature values of the Young's modulus, assuming a Poisson ratio of 0.3. For MCC, a relatively large range of values have been reported, with a typical value being about 7.5 GPa at zero porosity [27]. A recent determination of elastic properties of LAC has provided a value of about 5.0 GPa for the Young's modulus at zero porosity [27]. Based on the moduli for the constituent materials, the bulk modulus for the MCC/LAC composite particles was calculated as described in [28]. The normal force-displacement curves used in the simulations are provided in Fig. 4.

The tangential forces were inferred from a standard linear spring–dashpot model (stiffness 100 N/mm). In all simulations, the sliding friction coefficient was 0.5 between particles and 0.1 between a particle and a confining wall. Contact damping was used, with a fractional damping coefficient of 0.3. Rolling frictions coefficients of 1  $\mu\text{m}$  between particles and 0.2  $\mu\text{m}$  for particle-wall interactions were additionally included. The friction and damping coefficients have previously been used in DEM simulations of confined compression [14] and are considered to be representative for granules of the type investigated here [29]. To speed

up calculations, a particle-based linear approximation of the Voronoi volume was used, with intermittent exact volume calculations when needed [30].

## 5. Results and discussion

### 5.1 Granule characteristics

The characteristics of the investigated MCC and MCC/LAC granules are summarised in Table 2. The median particle size ( $d_{50}$ ) was somewhat larger for the MCC/LAC than for the MCC granules and both granule types had sizes in slight excess of the nominal sieve fraction (800–900  $\mu\text{m}$ ). As shown in Fig. 5, visual inspection of the granules revealed that the MCC granules were nearly spherical whereas the MCC/LAC granules were slightly elongated. Since the granules tend to position themselves in the most stable position during spreading on the flatbed scanner but can be arbitrarily oriented during sieving, deviations from a perfect spherical shape most likely explain the observed size difference between the granule types and why granule sizes in excess of the nominal sieve fraction were observed. These conclusions are corroborated by the Heywood (surface-volume) shape coefficient ( $\alpha_{SV}$ ), calculated as the product of the median particle size and the volume-specific external surface areas (Table 2). The Heywood shape coefficient assumes a value of 6 for spherical particles whereas values larger than 6 signify a deviation from a spherical shape. The values obtained were 6.7 for the MCC and 7.8 for the MCC/LAC granules (Table 2), confirming the elongation of the latter.

The intra-granular porosity, calculated from the apparent and the effective particle density (Table 2), was higher for MCC/LAC ( $\approx 18\%$ ) than for MCC ( $\approx 11\%$ ) granules. Whereas the

porosity of the MCC granules was in good agreement with previously published data, the porosity obtained for the MCC/LAC granules was higher than previously reported values [19]. This difference is presumably explained by batch variations for both the MCC and LAC powders. High porosity granules tend to be more prone to densification due to the large pore space available for plastic volume reduction [31, 32].

The bulk density for the MCC/LAC granules was slightly lower than for the MCC granules due to the higher intra-granular porosity and more irregular shape of the former [19]. After tapping, the bulk density increased slightly for both systems indicating an initial close packing after pouring. This was further confirmed by the low CI from which the granules were classified as excellent flowing [24]. The extragranular porosity (voidage) was about 40% for both granule types, as calculated from the bulk density and effective granule density. This value is lower than the ones obtained for the packings generated for the numerical simulations, for which the voidage was about 50%. This difference likely originates from boundary effects that are more prominent for the numerical packings which had a considerably smaller diameter and height.

The hardness ( $H$ ), estimated from the force-deformation relationship of single-granule compression, was significantly lower for the MCC/LAC than the MCC granules (Table 2).

The lower hardness of the MCC/LAC granules is explained by their higher porosity and their ductile-brittle nature.

## **5.2 Confined granule bed compression**

As displayed in Fig. 6, the pressure evolution during compression was different for the MCC and the MCC/LAC granules. A noticeable pressure increase occurred at a bed height slightly larger than 6 mm for the MCC granules and at about 7 mm for the MCC/LAC granules. Thereafter, a relatively linear increase in pressure with decreasing bed height was observed for both the MCC and MCC/LAC granules, followed by an extended non-linear region. The non-linear region can in a broad sense be interpreted as a crossover region between a predominantly plastic and a predominantly elastic deformation stage. The less rapid increase in pressure observed for the MCC/LAC granules at small to intermediate strains is explained by local fragmentation at the pellet surfaces, as expected for granules with ductile-brittle deformation characteristics [19], likely combined a larger degree of plastic volume reduction caused by their larger porosity [32].

A comparison between the experimental and numerical results is presented in Fig. 7a for the MCC granules and in Fig. 7b for the MCC/LAC granules. Considering firstly the ductile MCC granules (Fig. 7a), it can be noted that the experimental and numerical compressions were initiated at a similar granule bed height and that the linear increase in pressure was well captured by the simulations when plastic densification was accounted for (solid grey curve in Fig. 7a). However, the simulations predicted a less rapid increase in pressure at large strains and hence a lower height of the formed tablet. The simulations that were performed without an account of plastic volume reduction did, on the other hand, predict a more rapid increase in pressure at large strain and consequently a tablet height that exceeded the experimental one (dashed grey curve in Fig. 7a). Since the shape of the numerical curves nicely followed the experimental one, these results indicate that a residual porosity of about half the initial value remained in the pellets also at the highest applied pressures. This finding is consistent with prior experimental characterisations of retrieved granules post compression [31, 32].

Considering, secondly, the ductile-brittle MCC/LAC granules (Fig. 7b), it can be seen that the experimental and numerical compressions were initiated at a similar granule bed height, as for the MCC granules. However, both simulations started to deviate from the experiments at a relatively early stage. Both simulations predicted a more rapid pressure increase for intermediate strains and a more rapid crossover between predominantly plastic to predominantly elastic responses. These discrepancies are explained by the brittle characteristics of the granules which were not included in the numerical model. As for the MCC granules, the final tablet height was underestimated by the simulations that were performed with an account of plastic volume reduction (solid grey curve in Fig. 7b) and overestimated when plastic volume reduction was disregarded (dashed grey curve in Fig. 7b). Hence, a residual porosity most likely remained also for the MCC/LAC granules.

The increase in coordination number with decreasing granule bed height, as obtained from the simulations and displayed in Fig. 8, shed more light on the transitions between the stages that occur during compression. A granule rearrangement stage is apparent from the low and rapidly changing coordination number at high granule bed heights for both MCC and MCC/LAC granules. The rapid changes suggest that inter-particle contacts continuously form and break, i.e., the particles rearrange in-die. Rearrangement is expected to cease at the jamming transition, which for granular materials comprising frictional spherical particles has been reported to occur at a coordination number around 4.5 [33]. This value appears reasonable for both MCC and MCC/LAC as this corresponds to the knee on the curve immediately after the rearrangement (dashed horizontal line in Fig. 8). As expected, the rearrangement stage is independent of the propensity for plastic particle densification, since

the particles will not densify until they reach a constrained state. However, since each particle becomes smaller, the coordination number exhibits a less rapid increase when plastic particle densification is accounted for in the simulations.

A gradual change in slope of the coordination number vs. granule bed height curves is observed at a coordination number of about 9 (dotted horizontal line in Fig. 8). The increased slope likely reflects the closure of the last remaining pores in the vicinity of individual particles. Since this process immediately precedes the transition from predominantly plastic to predominantly elastic deformation for the affected particles, this deformation stage will be referred to as incipient elastic. The compact as a whole will start to deform elastically once a percolating network of elastically deforming particles has formed [14]. It can be noted that the tentative critical coordination number is about twice as large as the one corresponding to the jamming transition. However, this value should be considered as an indication as it is out of scope of this paper to analyse whether it can be used as a generic critical value for the transition to incipient elastic deformation.

## **6. Conclusions**

In this work, an extension of the truncated-sphere contact model was presented that accounted for plastic particle densification and utilised Voronoi cells to estimate the void space surrounding each particle. The model was implemented in the DEM and evaluated against bulk compression experiments for beds comprising ductile and ductile-brittle granules. Simulations were performed both with and without an account of the plastic particle densification. The model provided an adequate prediction of the powder compression profiles

obtained for the ductile particles, although the data indicated that a residual porosity remained in the granules also at the highest applied compression pressures. However, the agreement between experiments and simulations was less satisfactory for the ductile-brittle granules, indicating that fragmentation constituted an important compression mechanism for this system, as expected. It is concluded that the extended truncated-sphere model is suitable for and provides insight into the challenging task of describing confined powder compression at large strains for ductile particles. The model could for example be used to investigate the evolution in bonding area and tablet strength, issues that are central for pharmaceutical applications of powder compression. However, the model cannot reliably be applied to fragmenting systems unless a way be found to describe particle fracture.

## **Acknowledgements**

The authors wish to acknowledge the Swedish Research Council (Project No. 621-2011-4049) for financial support.

## **References**

- [1] P.A. Cundall, O.D.L. Strack, A discrete numerical model for granular assemblies, *Géotechnique*, 29 (1979) 47-65.
- [2] B. Storakers, S. Biwa, P.L. Larsson, Similarity analysis of inelastic contact, *International Journal of Solids and Structures*, 34 (1997) 3061-3083.
- [3] C. Thornton, Z.M. Ning, A theoretical model for the stick/bounce behaviour of adhesive, elastic-plastic spheres, *Powder Technology*, 99 (1998) 154-162.
- [4] L. Vu-Quoc, X. Zhang, An elastoplastic contact force-displacement model in the normal direction: displacement-driven version, *Proceedings of the Royal Society a-Mathematical Physical and Engineering Sciences*, 455 (1999) 4013-4044.
- [5] M.R. Brake, An analytical elastic-perfectly plastic contact model, *International Journal of Solids and Structures*, 49 (2012) 3129-3141.
- [6] O.R. Walton, R.L. Braun, Viscosity, antigranulocytes-temperature, and stress calculations for shearing assemblies of inelastic, frictional disks *Journal of Rheology*, 30 (1986) 949-980.
- [7] S. Luding, K. Manetsberger, J. Mullers, A discrete model for long time sintering, *Journal of the Mechanics and Physics of Solids*, 53 (2005) 455-491.

- [8] G.D. Scott, D.M. Kilgour, Density of random close packing of spheres, *Journal of Physics D-Applied Physics*, 2 (1969) 863-866.
- [9] S.D. Mesarovic, N.A. Fleck, Frictionless indentation of dissimilar elastic-plastic spheres, *International Journal of Solids and Structures*, 37 (2000) 7071-7091.
- [10] B. Harthong, J.F. Jerier, P. Doremus, D. Imbault, F.V. Donze, Modeling of high-density compaction of granular materials by the Discrete Element Method, *International Journal of Solids and Structures*, 46 (2009) 3357-3364.
- [11] J.F. Jerier, B. Harthong, V. Richefeu, B. Chareyre, D. Imbault, F.V. Donze, P. Doremus, Study of cold powder compaction by using the discrete element method, *Powder Technology*, 208 (2011) 537-541.
- [12] B. Harthong, J.F. Jerier, V. Richefeu, B. Chareyre, P. Doremus, D. Imbault, F.V. Donze, Contact impingement in packings of elastic-plastic spheres, application to powder compaction, *International Journal of Mechanical Sciences*, 61 (2012) 32-43.
- [13] M. Gonzalez, A.M. Cuitino, A nonlocal contact formulation for confined granular systems, *Journal of the Mechanics and Physics of Solids*, 60 (2012) 333-350.
- [14] A.-S. Persson, G. Frenning, An experimental evaluation of the accuracy to simulate granule bed compression using the discrete element method, *Powder Technology*, 219 (2012) 249-256.
- [15] E. Olsson, P.L. Larsson, A numerical analysis of cold powder compaction based on micromechanical experiments, *Powder Technol.*, 243 (2013) 71-78.
- [16] G. Frenning, Towards a mechanistic model for the interaction between plastically deforming particles under confined conditions: a numerical and analytical analysis, *Materials Letters*, 92 (2013) 365-368.
- [17] E. Arzt, The influence of an increasing particle coordination on the densification of spherical powders, *Acta Metallurgica*, 30 (1982) 1883-1890.
- [18] E. Jerwanska, G. Alderborn, J.M. Newton, C. Nyström, The effect of water-content on the porosity and liquid saturation of extruded cylinders, *Int. J. Pharm.*, 121 (1995) 65-71.
- [19] J. Nordström, K. Welch, G. Frenning, G. Alderborn, On the physical interpretation of the Kawakita and Adams parameters derived from confined compression of granular solids, *Powder Technology*, 182 (2008) 424-435.
- [20] M.D. Abramoff, P.J. Magelhaes, S.J. Ram, *Image Processing with ImageJ*, *Biophotonics International*, 11 (2004) 36-42.
- [21] M. Eriksson, C. Nyström, G. Alderborn, The use of air permeametry for the assessment of external surface area and sphericity of pelletized granules, *International Journal of Pharmaceutics*, 99 (1993) 197-207.
- [22] M. Wikberg, G. Alderborn, Compression characteristics of granulated materials II. Evaluation of granule fragmentation during compression by tablet permeability and porosity measurements, *International Journal of Pharmaceutics*, 62 (1990) 229-241.
- [23] European Pharmacopoeia 7th Edition, Monograph 2.9.34. Bulk and tapped density of powders, Directorate for the Quality of Medicines of the Council of Europe, Strasbourg, 2010.
- [24] R.L. Carr, Evaluating flow properties of solids, *Chemical Engineering*, 72 (1965) 69-72.
- [25] R.L. Jackson, I. Green, A finite element study of elasto-plastic hemispherical contact against a rigid flat, *Journal of Tribology-Transactions of the Asme*, 127 (2005) 343-354.
- [26] E.J. Abbott, F.A. Firestone, Specifying surface quality - a method based on accurate measurement and comparison, *Mechanical Engineering*, 55 (1933) 569-572.
- [27] K.M. Alston, Mechanical property variability in lactose monohydrate, Purdue University, Ann Arbor, 2012.
- [28] Z. Hashin, S. Shtrikman, A variational approach to the theory of the elastic behaviour of multiphase materials, *Journal of the Mechanics and Physics of Solids*, 11 (1963) 127-140.
- [29] A.-S. Persson, G. Alderborn, G. Frenning, Flowability of surface modified pharmaceutical granules: A comparative experimental and numerical study, *European Journal of Pharmaceutical Sciences*, 42 (2011) 199-209.

- [30] G. Frenning, Efficient Voronoi volume estimation for DEM simulations of granular materials under confined conditions, *MethodsX*, 2 (2015) 79-90.
- [31] J. Nordström, A.-S. Persson, L. Lazorova, G. Frenning, G. Alderborn, The degree of compression of spherical granular solids controls the evolution of microstructure and bond probability during compaction, *International Journal of Pharmaceutics*, 442 (2013) 3-12.
- [32] B. Johansson, G. Alderborn, Degree of pellet deformation during compaction and its relationship to the tensile strength of tablets formed of microcrystalline cellulose pellets, *International Journal of Pharmaceutics*, 132 (1996) 207-220.
- [33] H.P. Zhang, H.A. Makse, Jamming transition in emulsions and granular materials, *Physical Review E*, 72 (2005).

## Figures

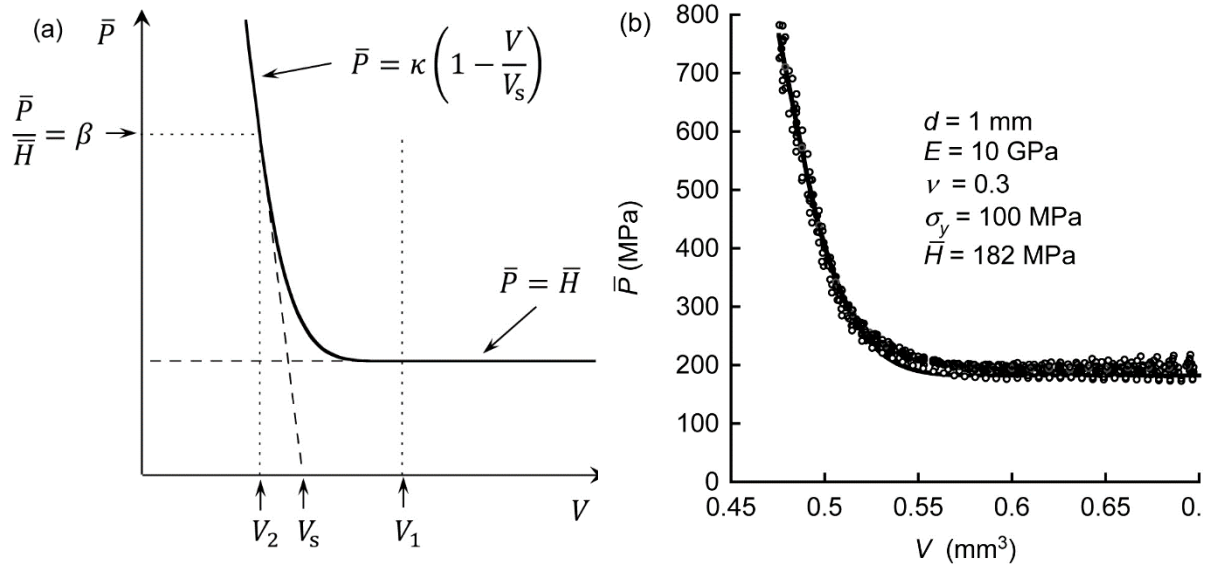


**Figure 1:** Dependence of the mean contact pressure  $\bar{P}$  on the Voronoi volume  $V$ . (a) Schematic illustration indicating the influence of the effective hardness  $\bar{H}$  and bulk modulus  $\kappa$  using the parameters  $\beta$ ,  $V_s$ ,  $V_1$  and  $V_2$  described in the text. (b) Comparison between  $\bar{P}$  as obtained from Eq. (2) using the parameter values  $\alpha = 5$  and  $\beta = 3$  (thick solid line) and numerical results (symbols) from triaxial loadings with different loading rates in the three spatial directions [16]. Parameter values are indicated in the figure ( $d$  = particle size,  $E$  = Young's modulus,  $\nu$  = Poisson's ratio,  $\sigma_y$  = yield stress and  $\bar{H}$  = effective hardness).

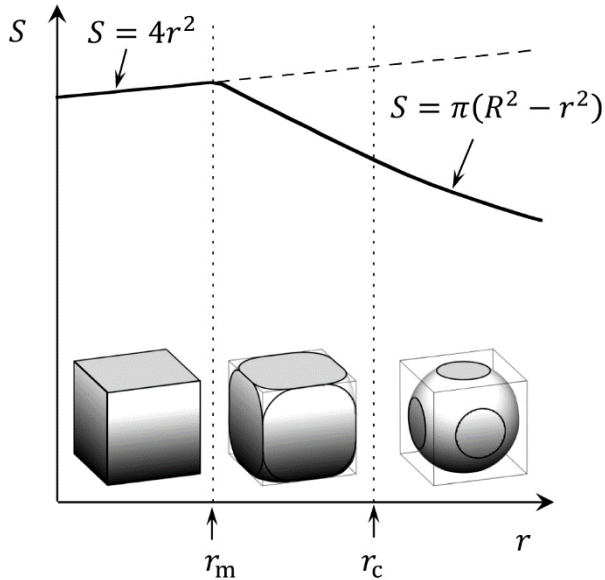


**Figure 2:** Schematic illustration of the procedure used to determine the contact area  $S$  for hydrostatic triaxial loading. As indicated, the area was inferred from a truncated sphere of radius  $R$  as long as the distance  $r$  between the particle centre and contact point was larger than a critical value  $r_c$ . The contact area was thereafter extrapolated until a second critical value  $r_m$  was reached, and from this junction, the Voronoi face area was used.

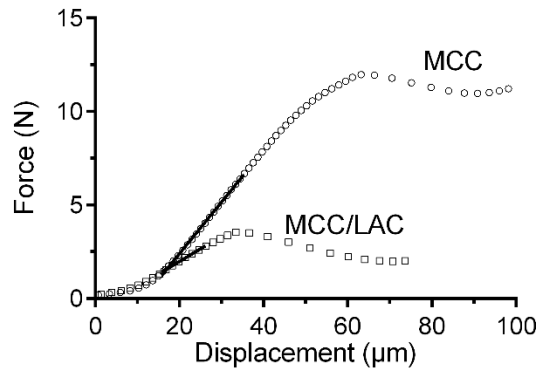


**Figure 3:** Typical force-displacement curves for MCC and MCC/LAC granules. The solid black lines represent linear fits to the data that were used to estimate the particle hardness.

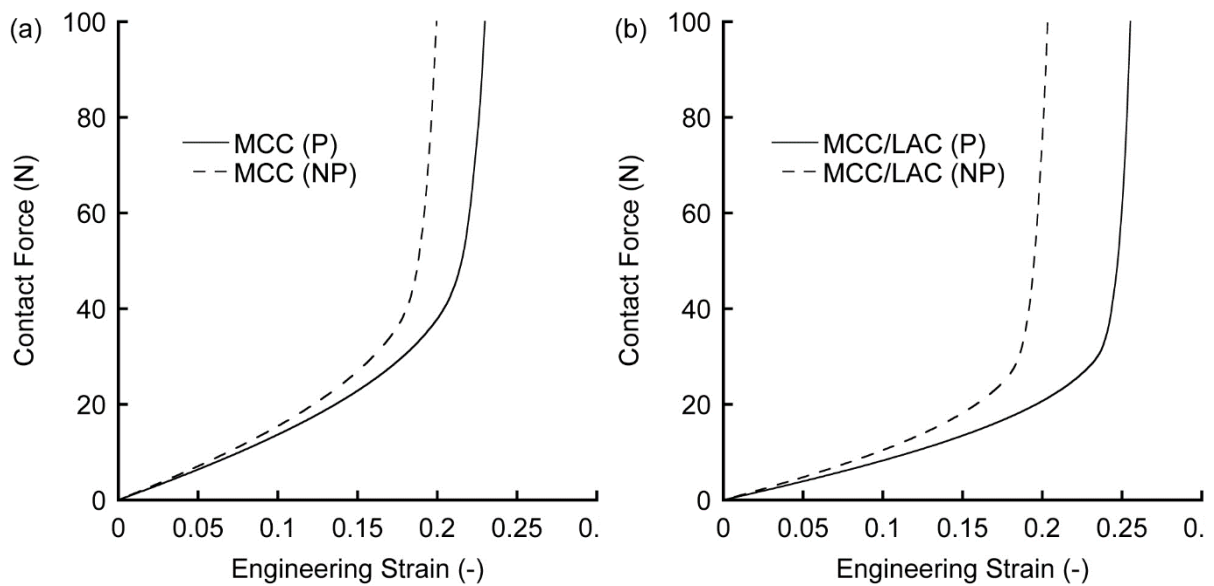


**Figure 4:** Normal contact force as a function of engineering strain for (a) MCC and (b) MCC/LAC granules with (P) and without (NP) an account of plastic particle densification.

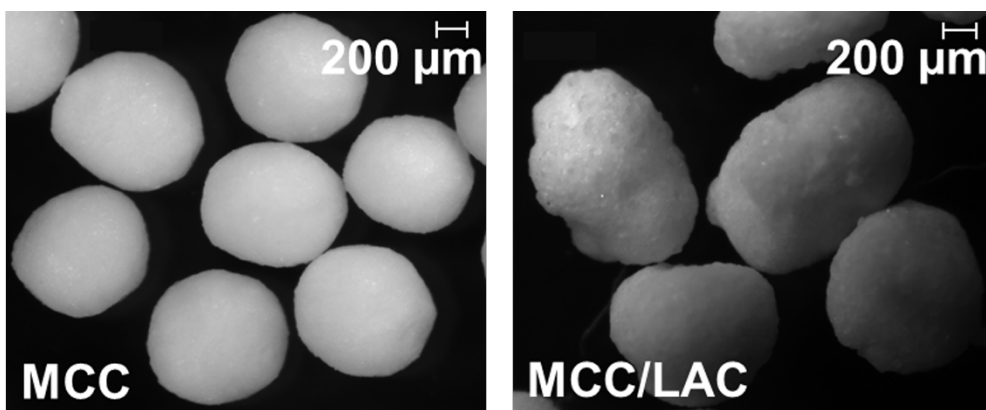


**Figure 5:** Microscopy images of MCC (left) and MCC/LAC granules (right) at 40 times magnification.

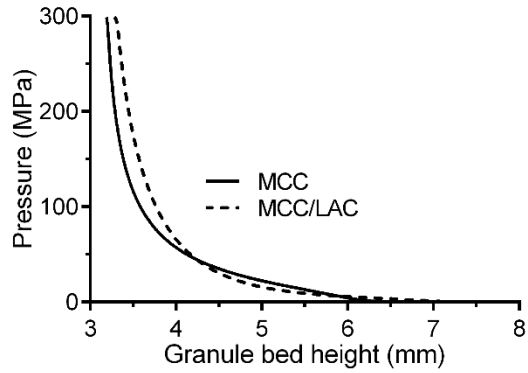


**Figure 6:** Pressure as a function of granule bed height for MCC and MCC/LAC granules.

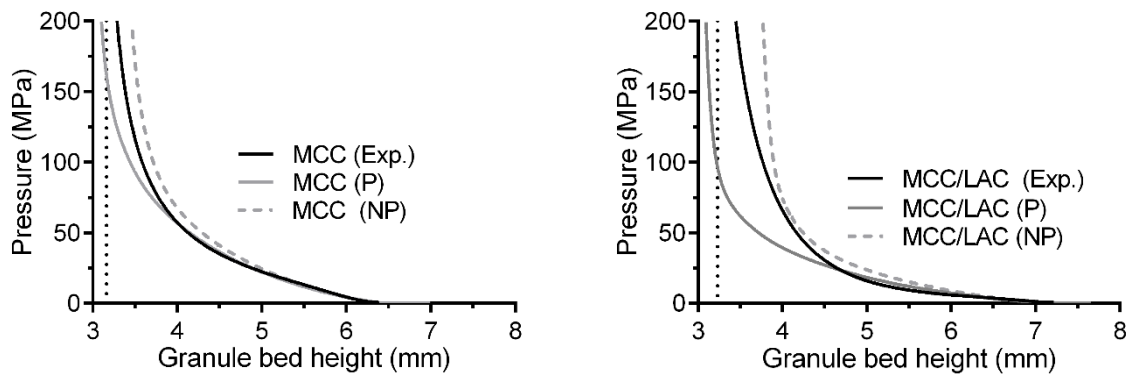


**Figure 7:** Comparison of experiments and simulations for (a) MCC and (b) MCC/LAC granules. Simulations were performed both with (P) and without (NP) an account of plastic particle densification. The dotted vertical lines indicate the height corresponding to zero porosity.

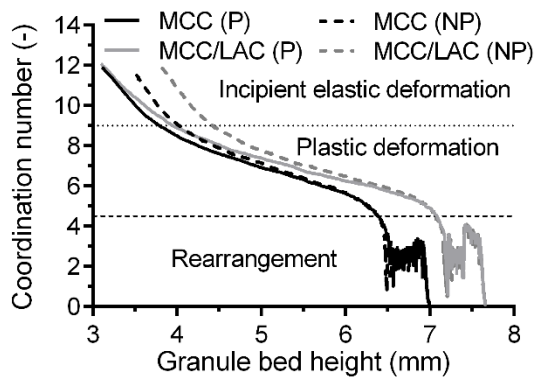


**Figure 8:** Coordination number as a function of granule bed height for MCC and MCC/LAC granules as obtained for simulations with (P) and without (NP) an account of plastic particle densification. The dashed horizontal line displays the transition between rearrangement and predominantly plastic deformation whereas the dotted horizontal line indicates the proposed transition between predominantly plastic and incipient elastic deformation.

## Tables

**Table 1:** Key parameters used in the simulations. The simulations are denominated by the granule type (MCC or MCC/LAC) and whether (P) or not (NP) an account has been made of plastic densification (in the latter case, they were treated as being nonporous).

Denomination	$R_{p0}$ (mm) <sup>a</sup>	$N_p$ (-) <sup>b</sup>	$\bar{H}$ (MPa) <sup>c</sup>	$\kappa$ (GPa) <sup>d</sup>	$\phi_0$ (%) <sup>e</sup>
MCC (P)	0.469	821	97.9	6.25	10.5
MCC (NP)	0.469	821	97.9	6.25	0.0
MCC/LAC (P)	0.522	662	53.1	4.17	17.9
MCC/LAC (NP)	0.522	662	53.1	4.17	0.0

<sup>a</sup> Initial particle radius.

<sup>b</sup> Number of .

<sup>c</sup> Effective hardness.

<sup>d</sup> Bulk modulus.

<sup>e</sup> Initial porosity.

**Table 2:** Granule characteristics. Standard deviations are given in parentheses.

Granule type	$d_{50}$ ( $\mu\text{m}$ ) <sup>a</sup>	$\rho_{\text{mix}}$ ( $\text{g}/\text{cm}^3$ ) <sup>b</sup>	$\rho_{\text{eff}}$ ( $\text{g}/\text{cm}^3$ ) <sup>c</sup>	$\rho_{\text{bulk}}$ ( $\text{g}/\text{cm}^3$ ) <sup>d</sup>	$\rho_{\text{tap}}$ ( $\text{g}/\text{cm}^3$ ) <sup>e</sup>	CI (%) <sup>f</sup>	$S_v$ ( $\text{cm}^{-1}$ ) <sup>g</sup>	$\alpha_{\text{SV}}$ (-) <sup>h</sup>	Porosit y (%)	$H$ (MPa) <sup>i</sup>
MCC	938.0	1.58 (0.002)	1.41 (0.004)	0.85 (0.01)	0.86 (0.01)	2.0 (0.0)	71.07 (0.60)	6.7	10.5 (0.24)	163 (16)
MCC/LAC	1043.4	1.55 (0.000)	1.27 (0.003)	0.74 (0.01)	0.77 (0.01)	3.3 (0.9)	74.27 (0.24)	7.8	17.9 (0.18)	88.5 (24)

<sup>a</sup> Median granule diameter.

<sup>b</sup> Apparent granule density.

<sup>c</sup> Effective granule density ( $n = 3$ ).

<sup>d</sup> Poured bulk density ( $n = 3$ ).

<sup>e</sup> Tapped bulk density ( $n = 3$ ).

<sup>f</sup> Carr's compressibility index ( $n = 3$ ).

<sup>g</sup> Volume specific surface area ( $n = 3$ ).

<sup>h</sup> Shape coefficient.

<sup>i</sup> Single-granule effective hardness ( $n = 50$ ).